Analysing the impact of far-out sidelobes on the imaging performance of the SKA-LOW telescope

Benjamin Mort,[1][*] Fred Dulwich,[1] Nima Razavi-Ghods,[2] Eloy de Lera Acedo[2] and Keith Grainge[3]

[1]*Oxford e-Research Centre, University of Oxford, 7 Keble Road, Oxford OX1 3QG, UK*
[2]*Cavendish Astrophysics, University of Cambridge, JJ Thomson Avenue, Cambridge CB3 0HE, UK*
[3]*School of Physics and Astronomy, University of Manchester, Alan Turing Building, Manchester M13 9PL, UK*

ABSTRACT

The Square Kilometre Array's Low Frequency instrument (SKA-LOW) will operate in the undersampled regime for most of the frequency band where grating lobes pose particular challenges. To achieve the expected level of sensitivity for SKA-LOW, it is particularly important to understand how interfering sources in both near and far side-lobes of the station beam affect the imaging performance. In this study, we discuss options for station designs, and adopting a random element layout, we assess its effectiveness by investigating how sources far from the main lobe of the station beam degrade images of the target field. These sources have the effect of introducing a noise-like corruption to images, which is called the far sidelobe confusion noise (FSCN). Using OSKAR, a software simulator accelerated using graphics processing units, we carried out end-to-end simulations using an all-sky model and telescope configuration representative of the SKA-LOW instrument. The FSCN is a function of both the station beam and the interferometric point spread function, and decreases with increasing observation time until the coverage of the aperture plane no longer improves. Using apodization to reduce the level of near-in sidelobes of the station beam had a notable improvement on the level of the FSCN at low frequencies. Our results indicate that the effects of picking up sources in the sidelobes are worse at low frequencies, where the array is less sparse.

Key words: instrumentation: interferometers – techniques: interferometric – telescopes.

1 INTRODUCTION

The Square Kilometre Array (SKA)[1], with its large collecting area and low receiver noise, has the potential to provide high fidelity, high dynamic range images over wide fields of view. In order to achieve its full potential, however, every aspect of the system will need to be analysed to unprecedented levels of detail. For the SKA's Low Frequency instrument (SKA-LOW), which will operate nominally in the 50–350 MHz frequency band and consists entirely of phased-array antennas, these requirements present significant challenges. Signals from the hundreds of fixed elements that make up each station will be combined electronically to form beams in the required direction. This leads to station beams that exhibit complicated behaviour as a function of frequency and scan angle, and hence the beams will change significantly over the course of an observation. As a phased-array telescope operating over such a wide bandwidth,

the configuration of the antennas in each station plays an important role in defining station sidelobe profiles, which have a direct impact on the performance of the instrument as an interferometer. For SKA-LOW, the spatial Nyquist frequency is typically around 80 MHz (Turner 2015), meaning that for the majority of the SKA-LOW band, the phased arrays are undersampling the incoming wave front. Sparse arrays give rise to grating lobes, which exhibit different behaviour for regular and irregular-type arrays, but in either case the presence of grating lobes implies that the beams formed at higher frequencies will be more sensitive to radiation from sources away from the direction of interest (Razavi-Ghods et al. 2012). The spilled power detected from sources in the sidelobes or grating lobes of the station beam has the effect of contaminating observations made of the target field, and thus will limit the image dynamic range if it cannot be removed adequately.

Whilst SKA pathfinder telescopes such as the Low Frequency Array (LOFAR; van Haarlem et al. 2013) and the Murchison Wide-field Array (MWA; Tingay et al. 2013) can test the use of aperture arrays at low frequencies, data sets from real instruments typically contain additional unwanted corruptions that can be difficult to deal

with, and these corruptions can mask other important effects. Simulations provide clean environments that allow us to understand and improve the SKA-LOW design. Notably, because the sensitivity of the SKA is expected to be so much higher than that of the pathfinders, effects that are negligible on those instruments may become critical for SKA.

In the first instance, a great deal may be learnt by attempting to optimize the configuration of the antenna positions and their weighting scheme within each station and by analysing the performance of individual stations (Razavi-Ghods et al. 2012; Clavier et al. 2014). However, this analysis must be extended to end-to-end simulations of the interferometer as a whole in order to understand how these station beam sidelobes can affect the resulting images (Smirnov et al. 2012).

End-to-end simulations of interferometers as large as SKA-LOW are extremely computationally intensive. Recent developments in simulation software, such as OSKAR[2], which evaluates the radio interferometer measurement equation (Hamaker 2006) using graphics processing units (GPUs) to give at least an order of magnitude improvement in performance over traditional simulation tools, make it possible to run large-scale, full-sky simulations of aperture arrays on reasonable time-scales.

In this paper, we present the results of an investigation in which we generated simulated visibilities using a large number of interfering sources far from the main lobe of the primary (station) beam of an SKA-like telescope consisting entirely of aperture arrays. These sources have the effect of introducing a noise-like corruption to images, known as the far sidelobe confusion noise (FSCN; Bregman 2004). Whilst many components of system noise behave like Gaussian random variables, and therefore tend to decrease as observation length increases, FSCN is due to a multitude of sidelobes from real sources that will not tend to zero simply by integrating for an infinite time. The amount of power introduced into the field is proportional to the sidelobe level of the point spread function (PSF) and the apparent flux I_a of each interfering source s in the element beam:

$$\text{FSCN} = \sum_s I_a \cdot \text{PSF}, \tag{1}$$

where all of these quantities are a function of source position, time and frequency. The level of the FSCN is therefore a function of both the aperture plane (UV) coverage and the overall ability of the interferometric cross-power station beam to act as an effective spatial filter on the sky.

The level of the FSCN can be reduced by removing the brightest and closest interfering sources using, for example, the CLEAN algorithm (Högbom 1974) or other source-peeling techniques if the emission from those sources can be modelled accurately. Removing the FSCN contribution of a source in this way requires excellent knowledge of the instrument to obtain both the apparent flux of the source, and an accurate PSF at the source position. Sparse aperture array stations, which naturally have more complex structure in their beam profiles than those from dish antennas or other filled apertures, give rise to apparent source fluxes that are higher and more variable away from the field of view. In practice, even if the instrument can be characterized very accurately, which is increasingly difficult far from the centre of the primary beam, the high-computational cost will eventually limit the number of sources that can be removed using this procedure, and a residual FSCN component will remain.

For a very sensitive instrument like the SKA, which will have exceptionally low thermal noise characteristics, FSCN may present a limiting factor in the noise performance for any science experiment that aims to remove all sources of contamination due to weak foregrounds.

We have chosen to use the FSCN as it proves a practical metric that tracks the performance of the aperture array station beams. Since the station beam has a considerable effect on the apparent source flux, apodization techniques can be used to improve the quality of the spatial filter the station beam provides. A sufficient level of control over the station beam sidelobes will be necessary for the SKA-LOW telescope, and this is described in Section 2. In Section 3, we describe the simulations we performed to study the level of the FSCN as a function of time and frequency using a representative SKA-LOW telescope model. In our analysis, we have also included a frequency of 650 MHz as a possible extended frequency band for SKA-LOW. We present the results of these simulations in Section 4. Finally, we discuss the implications of our results and present our conclusions in Section 5.

2 SKA-LOW ARRAY CONFIGURATION DESIGNS

The configuration of the antennas in an aperture array has been an active topic of research in radio astronomy for the past few years (Braun & van Cappellen 2006; Razavi-Ghods et al. 2012). Phased-array antenna systems may be implemented with regular as well as irregular geometries (Cappellen, Wijnholds & Bregman 2006). The former is well understood in the literature (e.g. Hansen 1998), especially in regards to the dense (separation $\leq \lambda/2$) and sparse (separation $> \lambda/2$) regimes where grating lobes are present.

Regular-type arrays consist of not only typical regular or hexagonal lattices, but also aperiodic array types, which can range from the Danzer or Penrose tiles to the more exotic snowflake configurations. What is apparent for all such arrays is the formation of grating lobes when operating in the undersampled regime. In this regime, a regular array would result in grating lobes, whilst below this frequency the array behaves very much like a continuous aperture. At a higher operating frequency where the array is sparser, the number of grating lobes increases and they also move closer to the main beam. Modern wideband array antennas, such as those proposed for the SKA, may be implemented with irregular/random configurations to decrease grating lobes when working in the sparse regime (Razavi-Ghods et al. 2012). However, the power, which would form a grating lobe in a regular array, is redistributed into a broad region of weaker irregular sidelobes, which are visible at all wavelengths. This may reduce the quality of the beam and can have an impact on the calibration of the instrument.

For SKA-LOW, in order to meet the sensitivity requirements (Turner 2015), a sparse configuration is needed to meet constraints of cost. Due to the Galactic synchrotron emission dominating at the low frequencies, in order to maximize the array sensitivity without increasing the number of elements, enough space needs to be allocated to each antenna in the array so that mutual coupling does not limit their effective aperture (de Lera Acedo et al. 2011b, 2015). Furthermore, in order to deliver maximum brightness sensitivity, the filling factor of the SKA-LOW core must be as high as possible (Mellema et al. 2013). In the SKA-LOW core, all the individual antenna elements contribute to capture the relevant Fourier modes in a given angular scale; therefore, a higher filling factor will maximize the information collected from the sky. This imposes a filling factor requirement, which sets some limits on the distance between

---
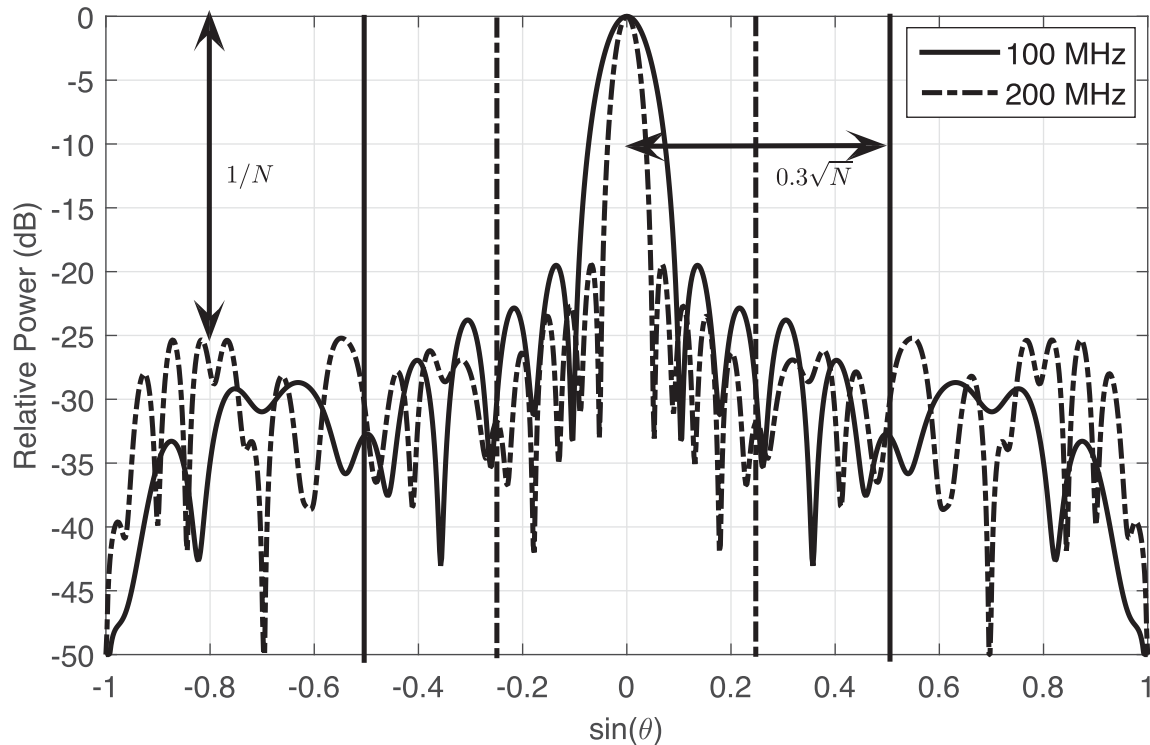
Figure 1. A cut of the typical expected SKA-LOW station beam incorporating the SKALA response at 100 and 200 MHz. The dotted lines show the transition region from dense to sparse.

elements and the required footprint per antenna. In the current design (Turner 2015), a trade-off average spacing between elements of ∼1.9 m has been chosen.

From the electromagnetic perspective, when discussing disconnected arrays as are proposed for SKA-LOW, antenna regularity will result in in-band resonances due to the mutual coupling of antennas, which cannot be avoided in wide band systems with bandwidths larger than 4:1. It can be observed that for the current SKA Log-periodic Antenna (SKALA), multiple in-band resonances appear when the antennas are placed in a regular configuration with $\lambda/2$ spacing at 100 MHz (de Lera Acedo et al. 2015).

For these reasons, it has been assumed that an irregular-type array must be implemented, i.e. one where the antenna positions are randomized. In a truly random array, the grating lobes would exist in the form of irregularly distributed sidelobes, which can be analysed by separating the array beam into so-called coherent and non-coherent regions. This terminology is described in detail in Clavier et al. (2014), where we estimate the boundary of this coherent to non-coherent region to appear after ∼$0.3\sqrt{N}$ sidelobes from the main beam, and the average level of sidelobes to be given by ∼$1/N$, where N is the number of antennas. For the SKA-LOW telescope, where each station contains nominally 256 antennas (Turner 2015), this transition would be ∼5 sidelobes from the main beam (Fig. 1) with the typical widths of sidelobes being $\lambda/2D$, where D is the diameter of the array. A higher operating frequency and thus more sparseness in a random array will result in this transition region appearing nearer the main beam in absolute terms. It is important to note that the sidelobe profile of each station may be different, since each station could use a different pseudo-random configuration. We explore this added advantage later.

When considering the effects of mutual coupling for a randomized array, studies have shown (Gonzalez-Ovejero et al. 2011; de

Lera Acedo et al. 2011a) that there is an averaging effect, which improves the more 'randomized' the positions of the antennas become and the greater the number of antennas in a given station. In Gonzalez-Ovejero et al. (2011), we show through EM simulations that the average of the embedded element patterns approaches the single (isolated) element pattern, and this is already apparent for only 256 antennas in a station (de Lera Acedo et al. 2011a). This is a great advantage when performing simulations of SKA-LOW, since this result means that it is possible to accurately model the station response to first order using a single isolated element pattern, which can be simulated using standard electromagnetic software simulation packages, such as COMPUTER SIMULATION TECHNOLOGY (CST).[3] This is the approach taken for the simulations presented in this paper. It is important to note that during calibration, the inclusion of an accurate account for these mutual coupling effects is critical in order to achieve dynamic ranges better than 60 dB (de Lera Acedo et al. 2013).

It has been demonstrated by the LOFAR High Band Antenna (HBA), which has regular phased-array stations, that by rotating the antenna positions, the grating lobes appear at different places on the sky. This results in the strong grating lobes of one station appearing where the response of the second station is low with the result that on multiplication, they average down dramatically in the power beam (Wijnholds, Bregman & van Ardenne 2011). For the SKA-LOW, we would also benefit from each array having a different random configuration and thus again resulting in the sidelobes of the station beam appearing at different positions on the sky, meaning in the interferometric sense that the contribution of faraway sources in the sidelobes can appear reduced.

---

[3] http://www.cst.com
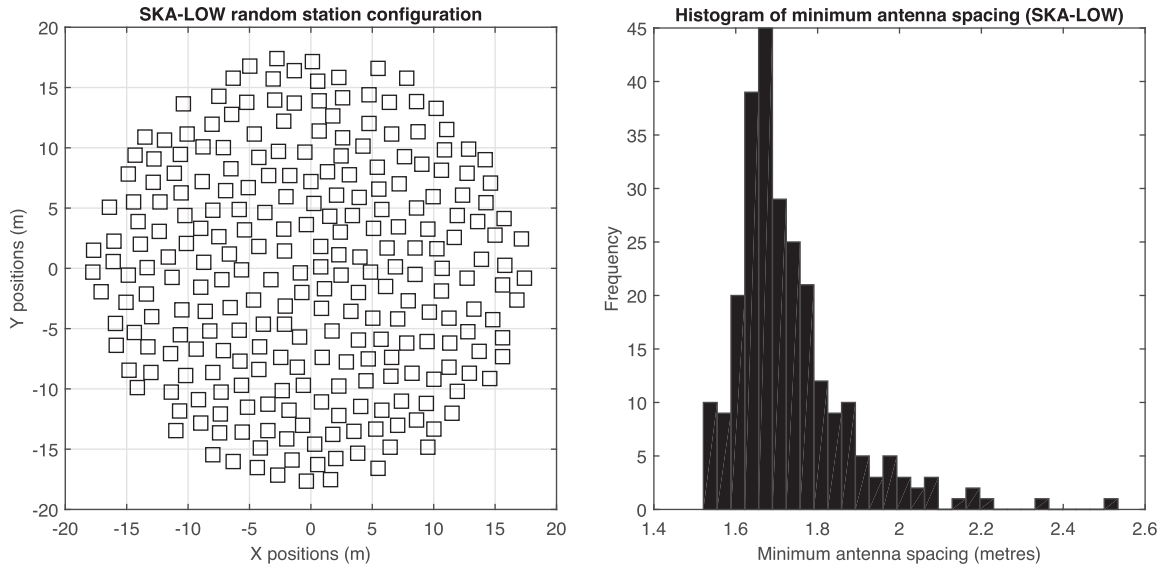
Figure 2. An example of an SKA-LOW random station (left) and the corresponding histogram of minimum antenna spacing (right).

2.1 Array layout and optimization for control of sidelobes

The placement of antennas in a pseudo-random array can be achieved by defining a minimum distance parameter, d_{min}, and placing antennas randomly in a defined perimeter, excluding any antennas which violate this distance to any surrounding antennas. It is also clear that d_{min} relates to the desired filing factor for a given array size. The smaller this number is, given the physical dimensions of the antenna, the more randomized the antenna positions become. This is not only beneficial from the mutual coupling perspective but also because the locations of sidelobes will become more randomized. It is important to note, however, that since d_{min} is very much subject to the physical size of the antenna, the full benefits of randomization cannot be attained without compromising filling factor, and therefore brightness sensitivity as noted earlier (Mellema et al. 2013). For SKA-LOW, the average spacing between antennas is ∼1.9 m (35 m diameter with 256 antennas; Turner 2015). To illustrate this, Fig. 2 shows a typical SKA-LOW station's random configuration (given a d_{min} of 1.5 m) and the corresponding histogram of the minimum distance.

The fact that the antennas positions do not appear truly randomized and the majority of antennas remain in close proximity to each other results in the formation of some sidelobes which exhibit the behaviour of grating lobes in regular arrays. Therefore, they cannot be suppressed simply by spatial or weight tapering (except in the aforementioned coherent region of the beam). Despite this limitation, even if two configurations are generated using the same d_{min} parameter, the position and size of the sidelobes are not the same for each one.

An option for the SKA-LOW array configuration is to make the histogram in Fig. 2 as broad as possible. This can be achieved by making the d_{min} parameter itself a random spacing within some limit, such as 1.5–2.5 m. However, this will result in a reduced filling factor and is therefore not ideal for SKA-LOW. This is also described in Grainge (2014) by assuming that a regular array has its elements perturbed in some random fashion in order to smear out the grating lobes.

Another option is to optimize the positions of the antennas in the array in order to achieve a desired sidelobe response as studied in Cohanim, Hewitt & de Weck (2004) and Kogan (2000). In Clavier

et al. (2014), a method of optimizing the positions of the antennas was presented based on three crucial steps. The first was regarded as a spatial tapering step, which aimed to morph a desired configuration into one which could achieve the appropriate beamwidth on the sky, similar to amplitude tapering. The second and third steps moved the antennas locally and individually in order to achieve a desired sidelobe profile, all the time maintaining the minimum distance criteria, such that no antennas were placed closer than the physical limit. The aforementioned strategy notably improved as more degrees of freedom were given in the placement of antennas as previously mentioned. However, with a requirement of a close-packed array, which was Nyquist sampled at the bottom of the SKA-LOW band, this method would only achieve a modest level of improvement (naturally near the main beam). Furthermore, the benefits of averaging out the effects of mutual coupling as would be the case in a pseudo-random array [see Gonzalez-Ovejero et al. (2011)] would no longer apply.

2.2 Apodization schemes

One of the major advantages of employing phased arrays is the ability to electronically control the weights applied to the signals from each antenna, thus allowing the array's main beam and sidelobe profile to be modified. Whilst in the strictest sense, apodization will degrade sensitivity, as is shown in this paper for a large interferometric telescope such as SKA-LOW, it will also reduce the effects of picking up unwanted bright sources in the near-in or intermediate sidelobes. Array apodization techniques are very common in various fields including radar and remote sensing. An example of a Taylor (Taylor 1955) tapering function applied to the SKA-LOW station beam (assuming randomized positions) is shown in Fig. 3.

For SKA-LOW, we empirically estimate the reduction in sensitivity, S, given by a typical tapering method to be

$$S(SLL_{dB}) \approx 1.47 \cdot SLL_{dB} + 26 \text{(per cent)}.$$

For the example shown in Fig. 3, in order to reduce the first sidelobe to a level of −28 dB (azimuthally), thus providing a >10 dB improvement, the reduction in sensitivity is expected to be 15 per cent. Irrespective of such a modest reduction in sensitivity, such schemes can be vital to achieve the best interferometric
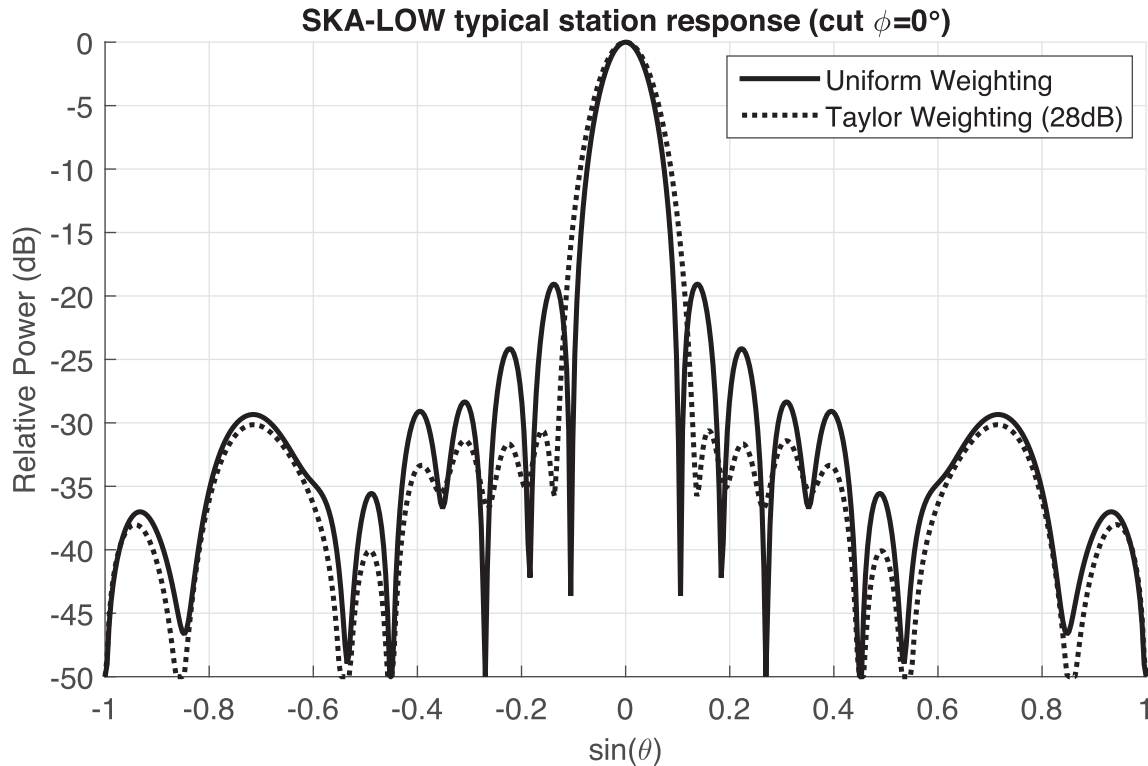
Figure 3. Typical SKA-LOW station response using a Taylor (28 dB) tapering method.

performance for large telescopes such as the SKA-LOW. This type of tapering is one which is analysed in this paper through end-to-end simulations.

Another method, described in Buisson & Razavi-Ghods (2015), adjusts the amplitudes of the elements to improve the array beam when working in the dense/sparse transition region. In Buisson & Razavi-Ghods (2015), the irregular array is first approximated as a continuous aperture, with one of the many well-known amplitude tapering patterns applied (e.g. Taylor, Gaussian). The elements are then treated as sampling the aperture and their amplitudes determined by the product of the amplitude of the continuous aperture at their location with an area factor. This area factor is related to the area occupied by each element. A number of definitions of occupied area may be used, including products of distances to nearest neighbours and the Voronoi cell division of the array. Such a technique is shown to provide improvements over standard tapering methods.

In Grainge (2014), there is a proposal for SKA stations in the core to be designed such that the station beam is not only comprised of beamforming 256 antennas but rather antennas out to $\sqrt{3}r_{full}$, where r_{full} is the baseline station radius of 17.5 m for SKA-LOW (Turner 2015). This implies using three times the number of antennas (768 elements) to form the station beam and using apodization to gain better control of the sidelobes, particularly near the main beam. Such a method of apodizing overlapping stations is also discussed in Razavi-Ghods et al. (private communication). Whilst this method implies losing a fraction of baselines, it does have a number of advantages, the main one being that the primary beam can have the same beamwidth as the un-apodized (non-overlapping) stations and therefore will result in very little loss in sensitivity. Furthermore, as described previously, the average far-out sidelobes are approximately given by $1/N$, where N is the number of antennas in a station, meaning a further 5 dB improvement can be achieved in the average level of sidelobes. In general, there is a considerable

choice over the weighting function in this scheme. One could even envisage keeping the beamwidth of the station response constant over a range of frequencies, for example in the EoR band.

Apodizing the station beam by re-weighting the antennas during beamforming has a similar effect to the visibility weighting schemes widely used in interferometric imaging, such as uniform, natural, Briggs (Briggs 1995) or adaptive (Yatawatta 2014) weighting. All of these schemes, whether applied to the station beam or the visibilities, trade sensitivity for sidelobe performance, but are commonly used to exploit data to their fullest.

3 INTERFEROMETER SIMULATIONS

In order to understand how the sidelobes of a phased-array affect the imaging capability of the SKA-LOW telescope, a number of simulations were carried out using the OSKAR simulator to assess the FSCN metric described in Section 1. The main simulation parameters, telescope model, and sky model used for these simulations are described below.

3.1 Telescope model

One of the main simulation parameters was the telescope model. Since no reference layout was available for the SKA-LOW telescope at the time of this study, a layout was generated to meet the requirements described in the SKA Level 1 Requirements Document (Turner 2015).

The layout used for our simulations contained 512 stations in total, with 470 stations within a 3 km radius of the centre of the array as shown in Fig. 4. This layout was based on a star-fish design described in Grainge (2014) with three spiral arms. Whilst such a layout will not provide the most optimal PSF or instantaneous
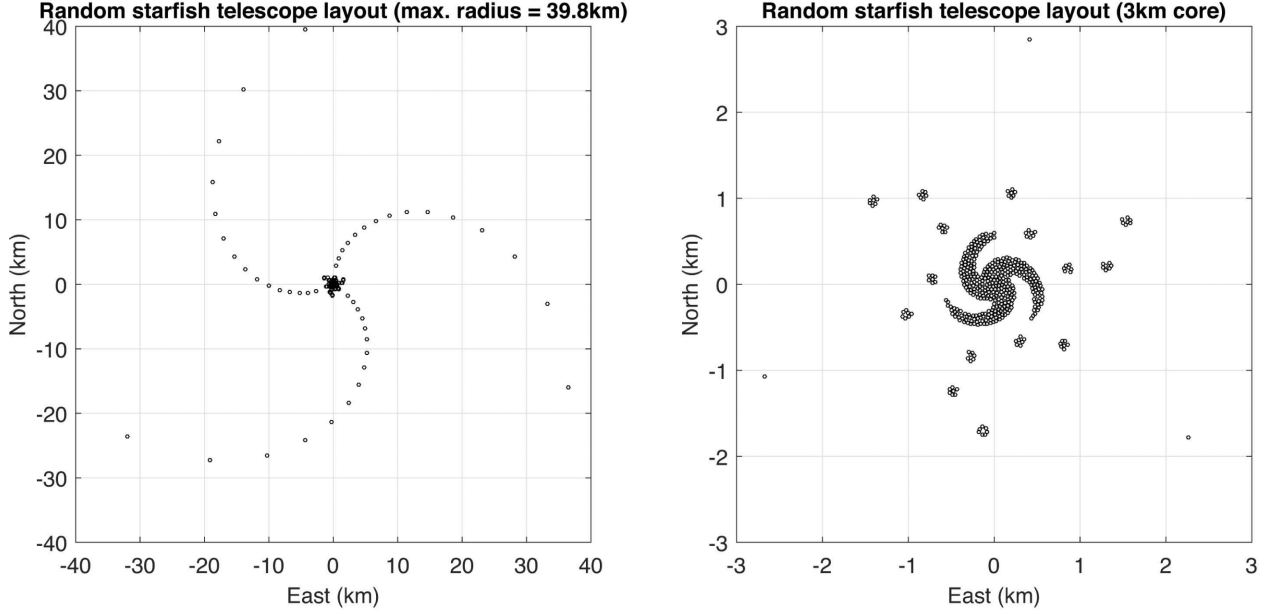
Random starfish telescope layout (max. radius = 39.8km)

Random starfish telescope layout (3km core)

Figure 4. An example telescope layout for SKA-LOW (left) and the core (right).

UV coverage, it is a realistic option from the point of view of implementation cost.

For the intra-station configuration, a different pseudo-random layout of 256 antennas was generated for each station, with the expectation that such an approach would minimize the effects of far-out sidelobes picking up unwanted bright sources in an interferometric sense as described in Section 2. Furthermore, our simulations included apodization of antenna weights using a 28 dB Taylor tapering function to change the characteristics of the station beams for comparison with the un-apodized case.

For the experiments that require the highest sensitivity over large angular scales (e.g. EoR experiments), the longer baselines in the configuration shown in Fig. 4 are likely to be used primarily for point source removal. For these simulations, a representative point source foreground would be removed as described in Section 3.2; therefore, there was justification in excluding the long baselines from this study. As such, the telescope model used in these simulations only included the 470 stations within 3 km of the core of the telescope.

In all our interferometer simulations, we used the patterns of the SKA Log-periodic Antenna (SKALA; de Lera Acedo et al. 2015) generated by full-wave simulations in the CST software package to evaluate the direction-dependent antenna response at the frequencies used for this study. Detailed electromagnetic studies of array antennas in randomized configurations (Gonzalez-Ovejero et al. 2011; de Lera Acedo et al. 2011a) show that the average embedded element patterns tend towards the isolated antenna pattern, and that the better the randomization of the antenna positions, the closer the agreement between the two. As discussed in Section 2, this benefit is not seen with any type of periodic arrays, and even some aperiodic configurations.

Plots showing the all-sky element responses in total intensity as well as images of the snapshot and time-averaged cross-power beams are shown in Fig. 5.

To estimate the thermal noise for this telescope, which was used for comparison with the FSCN, A_{eff} and T_{sys} were computed from full-wave array simulations, and included the clipping of effective aperture due to mutual coupling. The description of the calculations

is given in de Lera Acedo et al. (2015) and Cortes Medellin (1995). The sensitivity per element, on average, is given by

$$\frac{A_{eff}}{T_{sys}}\bigg|_{\theta,\phi} = \frac{\frac{\lambda^2}{4\pi}G_{\theta,\phi}}{\eta_{rad}T_A + (1 - \eta_{rad})T_0 + T_{rec}}, \quad (2)$$

where A_{eff} is the effective aperture, T_{sys} is the system temperature, λ is the wavelength, G is the gain of the embedded element in the array environment and η_{rad} is the radiation efficiency. Here T_A, T_0 and T_{rec} represent the antenna temperature, the ambient surrounding temperature (assumed 295K) and the receiver temperature, respectively. At the SKA-LOW frequencies, T_A is dominated by the Galactic synchrotron emission and follows the empirical law $T_{sky} \approx 60\lambda^{2.55}$ (e.g. Turner 2015), whilst T_{rec} is dominated by the matching between the low-noise amplifier and the antenna. For the entire SKA-LOW band, the system is dominated by the sky noise.

3.2 Sky model

Since the FSCN is a function of the position and brightness of sources in the sky, particular care was taken to use a representative sky model that would not strongly bias the results. However, as all-sky simulations of Galactic diffuse emission for an SKA-LOW sized telescope are unfeasible with current software, our sky model consisted entirely of discrete sources. The FSCN is most affected by bright sources close to the direction of interest, therefore for observations avoiding the bright Galactic plane, we do not expect this omission to have a significant influence on the results; however, assessing the impact of this fully is a desirable outcome of future work.

To evaluate the response from sources in the far sidelobes of the station beam, the sky model must fully populate the field of view of the antenna elements for the duration of each simulated observation. Since no catalogues of the full Southern hemisphere at the frequency of SKA-LOW were available when these simulations were carried out, we chose to use the re-reduced VLA Low-frequency Sky Survey (VLSSr) catalogue, version 2013-08-26 (Lane et al. 2014) as
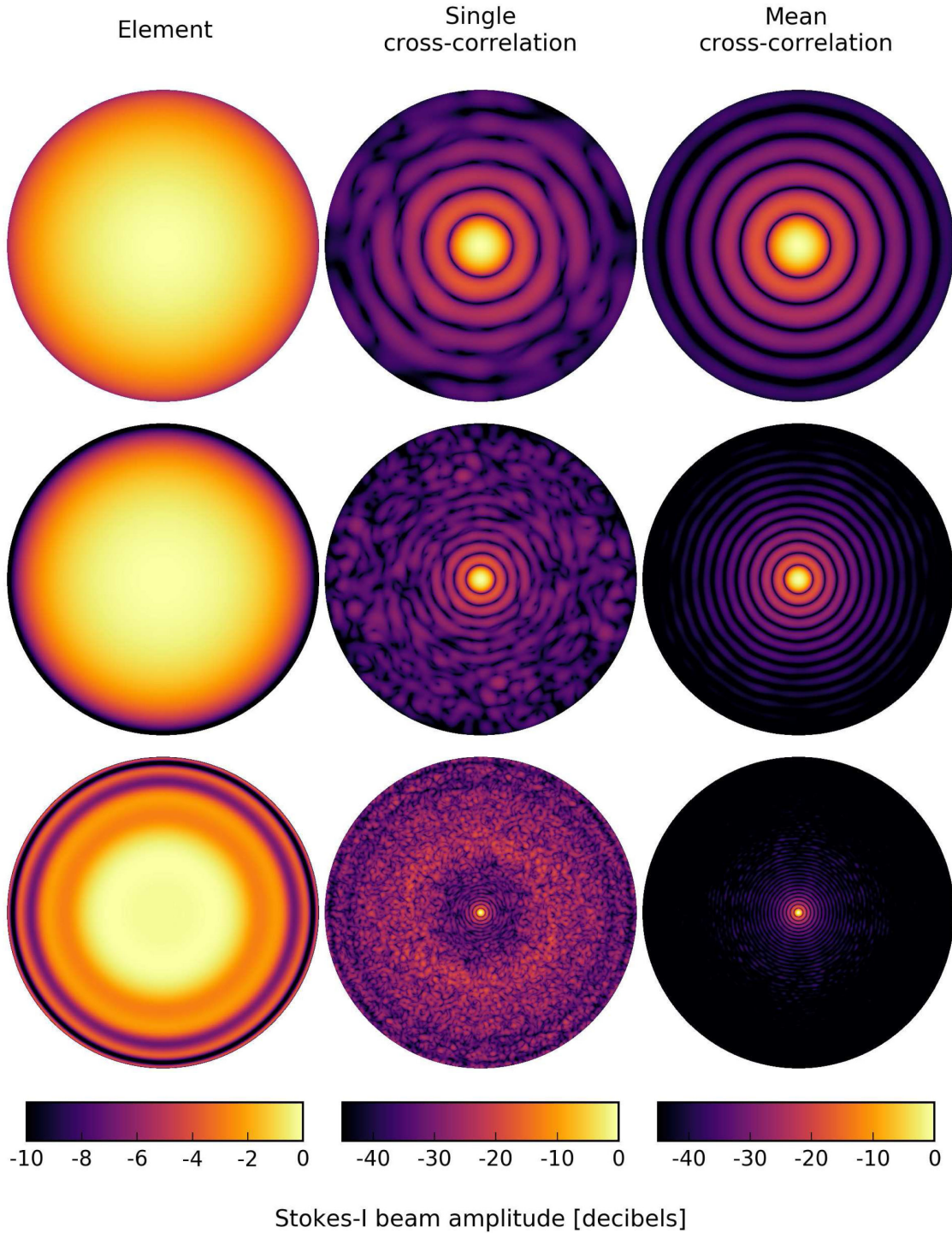
Figure 5. Plots showing the all-sky coverage of the Stokes-I element beam (left-hand column), the cross-power station beam for a single baseline (middle column), and the average cross-power station beam for the whole instrument (right-hand column) at 50 MHz (top row), 110 MHz (middle row) and 350 MHz (bottom row).

the basis for our all-sky model. VLSSr provides a larger total source count and improved source flux estimates over the original VLSS catalogue (Cohen et al. 2007). The survey covers the sky at declinations north of −30°, at 74 MHz. As VLSSr contains sources in the opposite hemisphere to SKA-LOW, we inverted the sign of the declination in the catalogue resulting in a statistically representative model of the southern sky. In future simulations, we intend to

make use of the MWA GLEAM source catalogue of the southern sky (Wayth et al. 2015).

Any processing pipeline used for the future SKA data will likely need to carefully remove the emission associated with the brightest sources, regardless of how far those sources are from the target field. In the LOFAR pipeline, this stage is called 'demixing' (van der Tol, Jeffs & van der Veen 2007). To simulate a perfect demixing process

in the simplest way, we removed the brightest sources from the VLSSr catalogue prior to the simulations. Sources with large angular size and significant structure are represented in both VLSS and VLSSr using multiple components, all of which must be removed during demixing. By searching the original VLSS catalogue data for groups of source components that overlap on the sky, Helmboldt et al. (2008) identified 388 sources with peak fluxes >15 Jy beam^{-1} at 74 MHz, and presented radio frequency spectra for each. To find these groups, the boundary of each component was treated as an ellipse with the same position and position angle as that given by the Gaussian fit, and extending 3σ from the centre. Components with boundaries that intersected were considered to be overlapping, so the peak flux of the source was then determined to be the component in the group with the largest peak flux. We repeated the procedure of Helmboldt et al. (2008) but using the VLSSr catalogue data, and with 5σ component widths rather than 3σ to ensure that no components of bright sources would be omitted.

After this process, the sky model contained 92 098 source components. In total, 598 components were removed from 424 bright sources with peak flux >15 Jy beam^{-1} in the VLSSr catalogue. Sources that were listed with only an upper bound to their deconvolved sizes were treated as point sources for this work. The total integrated flux from all components removed was ∼60 kJy, leaving ∼154 kJy at 74 MHz. For the remaining components, the minimum, maximum, mean and standard deviation of the integrated fluxes were 0.3, 36, 1.7 and 1.9 Jy, respectively. A spectral index value for each component was then randomly generated assuming a Gaussian probability distribution with mean and standard deviation taken from the 388 sources listed in Helmboldt et al. (2008). The mean spectral index was −0.92, and the standard deviation was 0.22.

In addition to the demixing process, we removed sources within the field of view out to the edge of the second sidelobe in order to emulate the CLEAN procedure that would be used to process real data. We simulated the operation of CLEAN down to a 3σ noise level of the telescope, based on a 6 h observation length and appropriate bandwidth, using the levels given by models of the antenna effective area. Thermal noise values were then derived from these. Sources were removed based on their apparent fluxes, which were determined using the average cross-power Stokes I beam for the whole observation duration. Because we removed sources out to the second sidelobe, the removal radius was scaled with frequency. At 50 MHz, between 4000 and 5000 sources were removed within a radius of 33°, and at 650 MHz, about 10 were removed within a radius of 2.5°. Exact numbers depended on the direction of the target field. This is illustrated in Fig. 6.

In practice, the number of sources that can be removed will be limited by the available compute power. As a result, we removed the same number of sources for the apodized station beams as that for the un-apodized stations to represent the same computational cost of post-processing in both cases. Although the numbers removed were the same, precisely which sources were removed still depended on their apparent flux, and therefore also their positions in the beam.

3.3 Observation parameters

In order to study the FSCN as a function of time and frequency, we selected six frequencies ranging over the whole extended SKA-LOW band. These were 50, 70, 110, 170, 350 and 650 MHz. The frequencies were not evenly distributed because we wanted to focus our attention on the dense–sparse array transition, whilst also investigating the high-frequency behaviour. We simulated a series of

single pointing observations, observing for lengths of time between 10 s and 8 h, distributed roughly evenly in log space. Each of these observations was assigned a symmetric range of hour angles, so that the phase centre would transit the meridian at the mid-point of the observation. As the sky model was relatively sparse, with a mean density of approximately 3 sources deg^{-2}, we generated a set of six target fields to ensure the sidelobe pattern from every station would be sampled adequately when assessing the mean FSCN value of these fields. Pointing directions for each of these six fields were chosen from a random distribution, with a selection criteria ensuring that the target fields did not drop below 45° in elevation in a 6 h observation of the target. The simulations include a thorough treatment of station beam effects by re-evaluating every station beam throughout the observation. Time and bandwidth smearing were chosen for critical (or supercritical) sampling on baselines in the core at the frequencies used for SKA-LOW, so we used a channel bandwidth of 73.2 kHz (4096 channels over the 300 MHz band) and 10.6 s integration time.

4 SIMULATION RESULTS

To post-process the simulated visibility data, we generated dirty images using both uniform (inverse-density) and natural (unmodified) visibility weighting schemes in the WSCLEAN software package (Offringa et al. 2014), where the image diagonal spanned the full-width-half-power of the station beam. The image sizes therefore scaled inversely with frequency. Because all the fields contained no sources out to the second sidelobe of the station beam, and because no thermal noise was added to the simulated visibilities, the RMS noise in these dirty images represents the noise floor due to the sources across the sky that cannot be removed easily using traditional methods.

4.1 Time scaling of FSCN

The level of FSCN as a function of observation length is shown in Fig. 7 (imaged with natural visibility weights) and Fig. 8 (imaged with uniform, or inverse-density UV weighting). The results of using un-apodized stations are shown in Figs 7(a) and 8(a), whilst the results of using station beams apodized using the 28 dB Taylor window are shown in Figs 7(b) and 8(b). For comparison, the straight, sloping lines on the plots show a simplistic model of the expected naturally weighted thermal noise in each case, which scales as the square root of the observation time. The estimated thermal noise on the Stokes-I dirty image was evaluated using:

$$\sigma_{\mathrm{image, thermal}} = \frac{2k_{\mathrm{B}}T_{\mathrm{sys}}}{\eta A_{\mathrm{eff}}\sqrt{4N_{\mathrm{b}}\Delta\nu\tau_{\mathrm{obs}}}}, \tag{3}$$

where k_{B} is the Boltzmann constant, T_{sys} is the system temperature, A_{eff} is the average station effective area, η is the efficiency of the station, N_{b} is the number of baselines, $\Delta\nu$ is the channel bandwidth and τ_{obs} is the observation length.

For simulated observations of up to about a length of 6 h, our data show that the level of the FSCN generally decreases with increasing observation length. This can be understood because the synthesized aperture becomes more filled, so the sidelobes of the interferometer's PSF become lower, and will therefore cause less power to be spilled into the target field.

If observing a given target for greater than 6 h, observations will include data from low elevations, and the effect of the antenna element starts to dominate the FSCN. Because the antennas are most sensitive at the zenith, the process of amplitude calibration
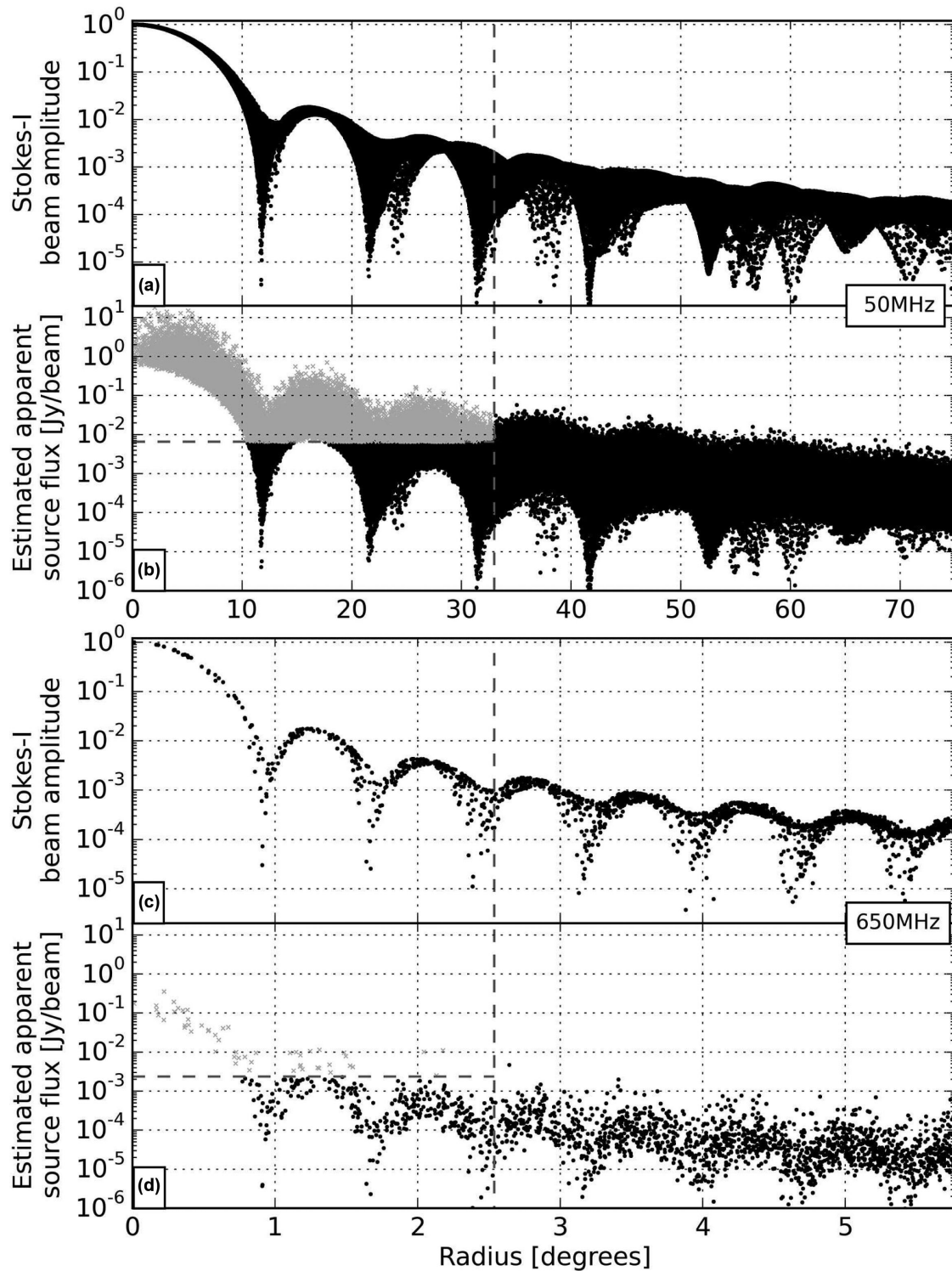
Figure 6. Emulation of a perfect 'CLEAN' source removal at 50 MHz (panels a and b) and 650 MHz (panels c and d; note the frequency-scaled *x*-axis values). For each simulation frequency, the average 6 h Stokes I cross-power beam of all 470 stations was evaluated at the position of all sources in the model (panels a and c) to estimate the apparent flux of each source (panels b and d). Sources of apparent flux above 3σ of the theoretical thermal noise for a 6 h observation (grey points) were then removed prior to the simulation.

for station beams that are much closer to the horizon means that the power from sources far away is increased relative to those near the phase centre, so the FSCN also starts to increase at lower target elevations. This is not an issue for the SKA-LOW, as observations will simply be selected to avoid low elevations. Target fields used in this study were chosen to be symmetric about the local meridian and not fall below 45° of elevation within the 6 h observation. The upturn in the FSCN can therefore simply be thought of as an indicator as the point at which the elevation of the target falls below the usable value for the antenna.
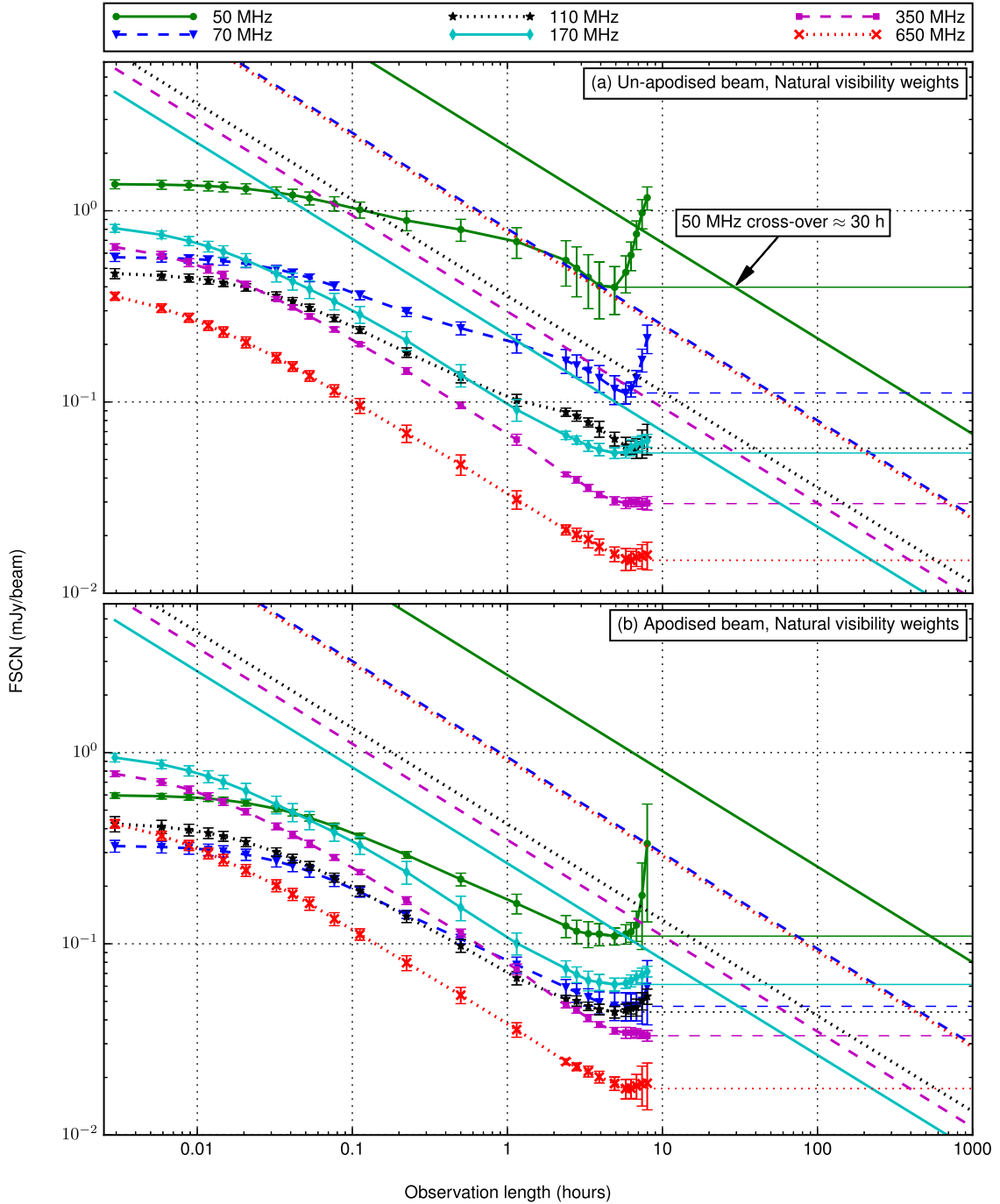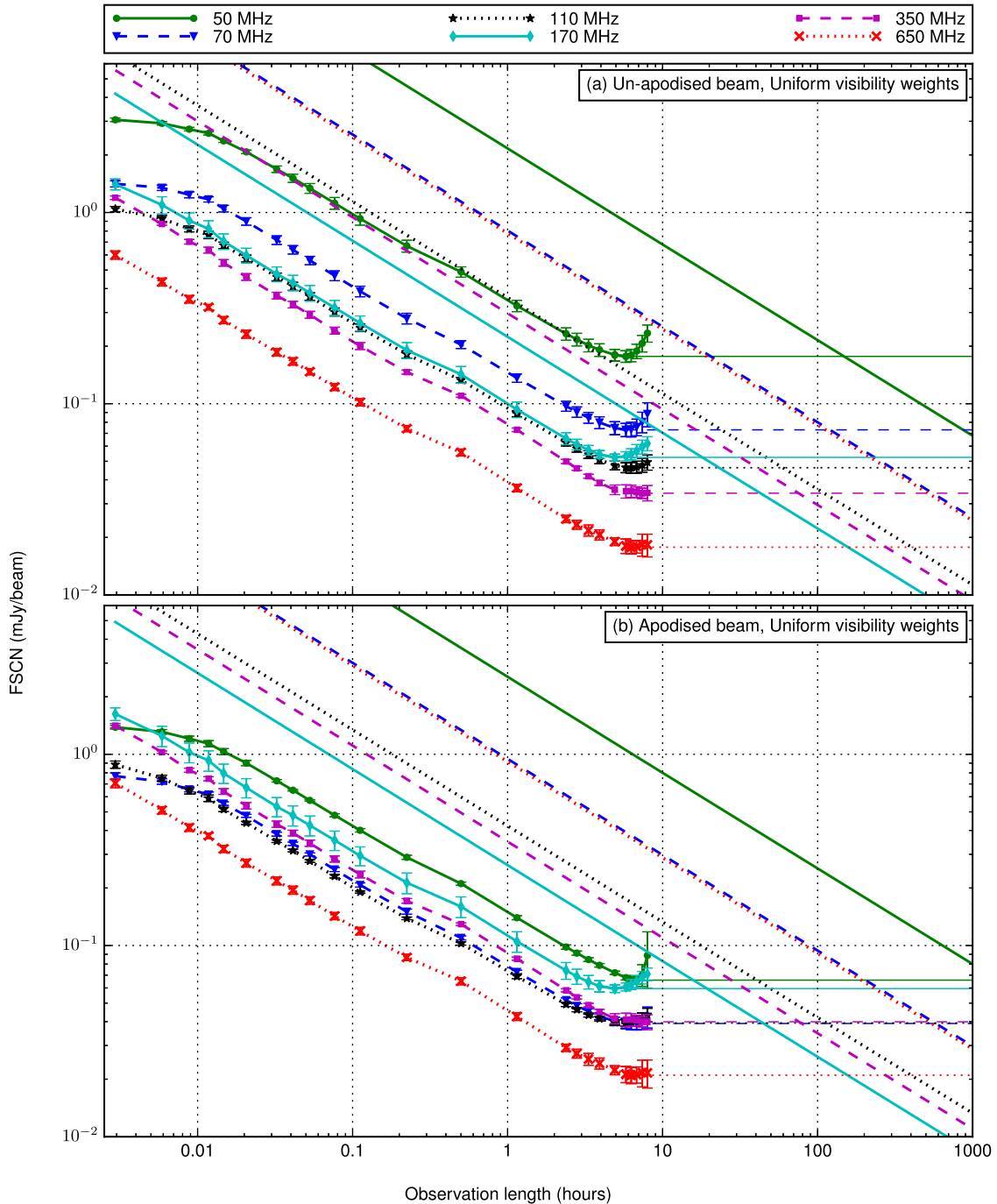
Figure 7. FSCN time scaling using natural visibility weighting for six observation frequencies using (a) un-apodized and (b) apodized stations. Error bars show the 1σ variation on the mean of the FSCN of six pointings. Straight sloping lines represent a simplistic naturally weighted thermal noise model. Horizontal lines illustrate an extrapolation from the estimated FSCN floor to longer observations.

By comparing Figs 7 and 8, we see that using uniform visibility weights causes the initial overall level of FSCN to become higher than when using natural visibility weights, but also causes it to scale better with observation time. Uniform weighting makes the sidelobes of the instantaneous PSF higher than natural weighting, because uniform weighting down-weights regions of the aperture plane which are more fully sampled. The re-weighting also has the effect of increasing the resolution by increasing the relative weight of the longer baselines. This explains why the FSCN is initially higher for uniform weighting, but the smaller spatial scale of the

sidelobes also means that they integrate towards zero faster: the smaller spatial scale means that summing the larger number of PSF sidelobes within the target field gives a better approximation to a normal distribution. Whilst apodizing the station beam reduces the effect of FSCN, particularly at low frequencies, the scaling behaviour with time does not change with apodization, as it is dominated by coverage of the aperture plane.

For long observations consisting of pointings made over multiple days, the thermal noise level will continue to decrease with time because it is simply Gaussian random noise. Since each new data

Figure 8. FSCN time scaling using uniform visibility weighting for six observation frequencies using (a) un-apodized and (b) apodized stations. Error bars show the 1σ variation between six pointings. Straight sloping lines represent a simplistic naturally weighted thermal noise model. Horizontal lines illustrate an extrapolation from the estimated FSCN noise floor to longer observations.

point is independent, thermal noise should always scale inversely with the square root of the integration time. However, unlike thermal noise, the level of the FSCN will not change significantly once the aperture plane becomes as filled as it can possibly be. Therefore, for a fixed set of baselines, the FSCN may well become the limiting factor to the telescope's sensitivity for an observation (or a series of observations) longer than 12 h, which is when the PSF will no longer improve due to Earth-rotation aperture synthesis. This limiting observation length may also be much less than 12 h depending on the declination of the source and the usable elevation range of

the aperture array. For the results of simulations plotted in Figs 7 and 8 a horizontal line has been drawn indicating the FSCN limit for the target fields being simulated in this study. By inspecting where this extrapolated line intercepts the thermal noise, one can obtain a rough estimate for the total accumulated observation length that a target can be observed before the noise becomes FSCN dominated.

As is indicated in Fig. 7, at 50 MHz, the thermal noise will reach the same level as our FSCN after only ∼30 h with this telescope configuration, using an un-apodized station beam with natural visibility weighting. Whilst this may appear concerning for deep
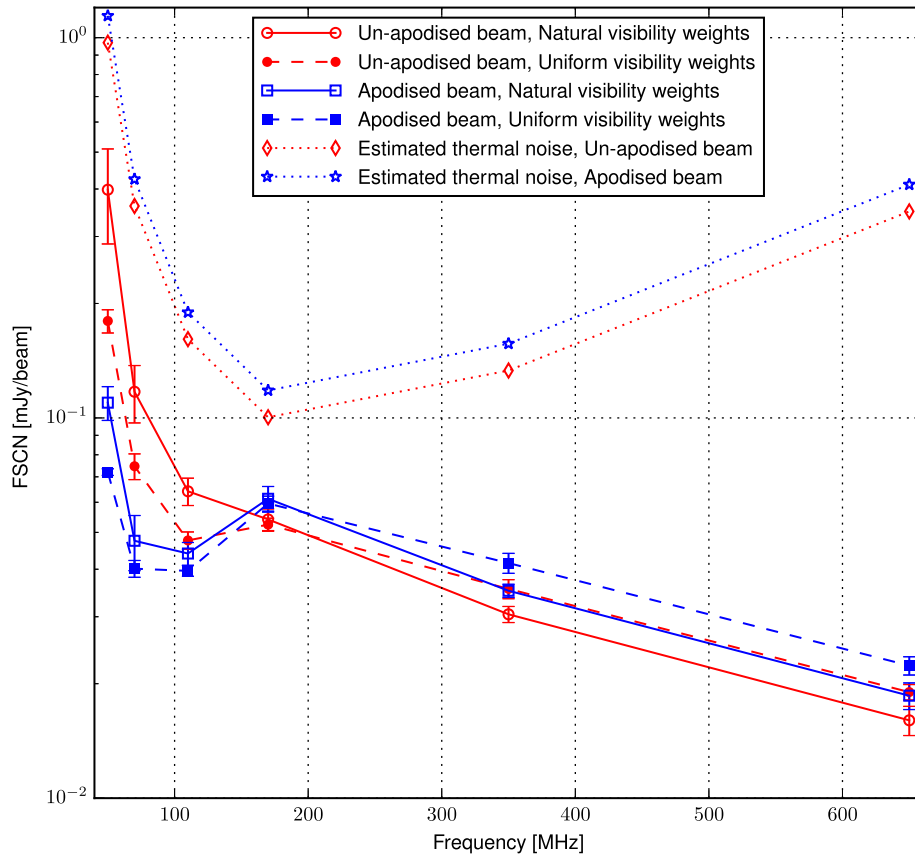
Figure 9. FSCN frequency scaling for a 17 702 s (∼5 h) observation, for both un-apodized station beams (circular symbols) and apodized station beams (square symbols), imaged using natural visibility weighting (solid lines/empty symbols) and uniform visibility weighting (dashed lines/filled symbols). The dotted lines show the estimated thermal noise for the observation. Error bars are drawn to show the 1σ variation between the six simulated pointings.

imaging experiments that would require thousands of hours of integration time to reach the required noise level (if thermal noise was assumed to be the only limit for those experiments), in practice, longer observations will very likely also involve subtracting more sources from the sky model. Although it is hard to extrapolate to a length of observation where this becomes a serious issue, the FSCN will eventually present a noise limit above the expected thermal noise. This is especially true because our simulations removed all sources in our sky model within the main lobe of the station beam, and there is a practical limit to the number of sources that can be removed for a reasonable post-processing cost.

4.2 Frequency scaling of the FSCN

The level of the FSCN as a function of frequency from 50 to 650 MHz, for a simulated observation length of 5 h, is shown in Fig. 9. Because all the stations are very sparse at the top end of the frequency band, it was reasonable to expect that the high level of grating lobes in the station beam would spill more power into the images from sources far away, but this is not what was observed. Generally, we observe that the level of the FSCN is inversely proportional to frequency, with the highest level of the FSCN at 50 MHz.

The reduction in the FSCN image RMS at higher frequencies can be explained by:

(i) The sky becoming fainter.
(ii) The primary beam (dominated by the array factor) becoming a more effective spatial filter on the sky with increasing frequency, thereby decreasing the total apparent flux of the sky.

(iii) The area on the sky sampled by the first few sidelobes of the primary beam decreases with increasing frequency as the beam gets narrower. Sources in this part of the beam make up a large contribution to the FSCN, and as the density of bright sources in the sky model remains constant, the FSCN contribution from the near in sidelobes decreases.

Fig. 9 demonstrates that a measurable component of the noise floor in any image, i.e. the FSCN, improves as a function of frequency. There is also a reduction in the level of the FSCN when using station beam apodization at low frequencies, although the opposite effect is observed at high frequencies. These results highlight the challenges SKA-LOW is likely to be faced with in terms of calibration and imaging at the low end of the band, where the wider station beam requires many more sources to be removed. Considering this metric alone, it is clear that imaging performance at 350–650 MHz should be no worse than at lower frequencies.

5 CONCLUSIONS

As our results have shown, the FSCN is a function of both the station beam and the interferometric PSF. Whilst the FSCN signal is not uncorrelated noise, it does decrease as observation time increases, up to the point where the UV coverage no longer improves or antenna directionality causes problems. Apodization of the station beam to reduce the level of the near-in sidelobes had a notable improvement on the level of the FSCN at low frequencies, and our

choice of apodization function was able to reduce the level of the FSCN by a factor of ~2 for only a 15 per cent loss in sensitivity. For this reason, it may be worth investigating whether frequency-dependent apodization would be worthwhile.

The FSCN is less than the thermal noise of the telescope over a 6 h observation, but we do not expect it to decrease at the same rate as a function of time. Improving the instantaneous aperture coverage, either by introducing more stations or adopting a less core-dominated configuration, would go some way to improving the FSCN, but this has cost implications and would reduce sensitivity to extended objects over the design used here. Without introducing more stations, another way to improve coverage of the aperture plane would be to adopt a reconfigurable station layout within the core, which allows the telescope to have a more fully filled aperture as observations continue beyond 12 h. For instance, dynamic logical regrouping of the elements into different stations could not only improve the shape and sidelobe cancellation of the station beams, but also create different sets of baselines which could help to keep the FSCN below the thermal noise. Maintaining the flexibility to do this by utilizing a 'sea' of elements in the core is therefore much more desired.

The FSCN does not indicate problems when using highly sparse arrays, which is not what one might expect. Because all stations have different randomized layouts, the resulting cross-power beam suppresses the far-out sidelobes of the station beam very well; and at higher frequencies, the main lobe of the station beam gets smaller and therefore acts as a better spatial filter on the sky. We note, however, that our sky model did not include diffuse emission from the Galaxy, and did not include sources down to a low-flux limit, so the sampling of the station beam sidelobes would have been worse at high frequencies as the beam became smaller. Future work using GLEAM (Wayth et al. 2015), which has a higher source count, would help to address this.

The effects of the ionosphere will act to reduce the FSCN by smearing sources as a function of time, but these effects were not included in this simulation. However, ionospheric effects will also make it harder to remove the brightest sources, unless the removal is done on very short time-scales. Smearing out sources is equivalent to replacing the bright sources with a larger population of weak sources, but the scaling of the FSCN in this regime requires further investigation.

Baseline dependent averaging (BDA), which is being actively investigated as an optimal form of compression for the huge volumes of visibility data produced by modern interferometers [e.g. Atemkeng et al. (2016)], should also have a beneficial effect on the FSCN. BDA results in increased smearing of sources far from the direction of interest, particularly on shorter baselines, and therefore will act to decrease FSCN. Simulating FSCN using a BDA pipeline would therefore be a an ideal direction for future study.

REFERENCES

Atemkeng M. T., Smirnov O. M., Tasse C., Foster G., Jonas J., 2016, MNRAS, 462, 2542
Braun R., van Cappellen W., 2006, preprint (astro-ph/0611160)
Bregman J. D., 2004, Exp. Astron., 17, 365
Briggs D., 1995, PhD thesis, New Mexico Institute of Mining and Technology
Buisson D. J. K., Razavi-Ghods N., 2015, in Graglia R. D., ed., Int. Conf. Electromagn. Adv. Appl. (ICEAA). Institute of Electrical and Electronics Engineers (IEEE). Torino, Italy
Cappellen W., Wijnholds S., Bregman J., 2006, 3rd Eur. Radar Conf. Institute of Electrical and Electronics Engineers (IEEE). Horizon House Publications Ltd, London
Clavier T., Razavi-Ghods N., Glineur F., Gonzalez-Ovejero D., de Lera Acedo E., Craeye C., Alexander P., 2014, IEEE Trans. Antennas Propag., 62, 1596
Cohanim B. E., Hewitt J. N., de Weck O., 2004, ApJS, 154, 705
Cohen A. S., Lane W. M., Cotton W. D., Kassim N. E., Lazio T. J. W., Perley R. A., Condon J. J., Erickson W. C., 2007, AJ, 134, 1245
Cortes Medellin G., 1995, US-SKA Technical Memo 95: Antenna Noise Temperature Calculations
de Lera Acedo E., Razavi-Ghods N., Ovejero D. G., Sarkis R., Craeye C., 2011a, in Graglia R. D., ed., Int. Conf. Electromagn. Adv. Appl. (ICEAA). Institute of Electrical and Electronics Engineers (IEEE). Torino, Italy
de Lera Acedo E., Razavi-Ghods N., Garcia L. E., Duffett-Smith P., Alexander P., 2011b, IEEE Trans. Antennas Propag., 59, 1808
de Lera Acedo E., Craeye C., Razavi-Ghods N., Gonzalez-Ovejero D., 2013, in Graglia R. D., ed., Int. Conf. Electromagn. Adv. Appl. (ICEAA). Institute of Electrical and Electronics Engineers (IEEE). Torino, Italy
de Lera Acedo E., Razavi-Ghods N., Troop N., Drought N., Faulkner A. J., 2015, Exp. Astron., 39, 567
Gonzalez-Ovejero D., de Lera Acedo E., Razavi-Ghods N., Craeye C., Munoz L. E. G., 2011, IEEE Int. Symp. Antennas Propag. (APSURSI). Institute of Electrical and Electronics Engineers (IEEE). IEEE
Grainge K., 2014, preprint (arXiv:1404.6184)
Hamaker J. P., 2006, A&A, 456, 395
Hansen R. C., 1998, Phased Array Antennas (Wiley Series in Microwave and Optical Engineering). Wiley, New York, Available at: https://books.google.co.uk/books?id=HaK6QgAACAAJ
Helmboldt J., Kassim N., Cohen A., Lane W., Lazio T., 2008, ApJS, 174, 313
Högbom J. A., 1974, A&AS, 15, 417
Kogan L., 2000, IEEE Trans. Antennas Propag., 48, 1075
Lane W. M., Cotton W. D., van Velzen S., Clarke T. E., Kassim N. E., Helmboldt J. F., Lazio T. J. W., Cohen A. S., 2014, MNRAS, 440, 327
Mellema G. et al., 2013, Exp. Astron., 36, 235
Offringa A. R. et al., 2014, MNRAS, 444, 606
Razavi-Ghods N., de Lera Acedo E., El-Makadema A., Alexander P., Brown A., 2012, Exp. Astron., 33, 141
Smirnov O. M., Frank B. S., Theron I. P., Heywood I., 2012, in Graglia R. D., ed., Int. Conf. Electromagn. Adv. Appl. (ICEAA), Institute of Electrical and Electronics Engineers (IEEE). IEEE, Cape Town
Taylor T., 1955, Trans. IRE Prof. Group Antennas Propag., 3, 16
Tingay S. J. et al., 2013, Publ. Astron. Soc. Aust., 30
Turner W., 2015, SKA-TEL-SKO-0000008, SKA Phase 1 System Level 1 Requirements (Rev 6)
van der Tol S., Jeffs B., van der Veen A.-J., 2007, IEEE Trans. Signal Process., 55, 4497
van Haarlem M. P. et al., 2013, A&A, 556, A2
Wayth R. B. et al., 2015, Publ. Astron. Soc. Aust., 32
Wijnholds S. J., Bregman J. D., van Ardenne A., 2011, Radio Sci., 46, RS0F07
Yatawatta S., 2014, MNRAS, 444, 790

This paper has been typeset from a TEX/LATEX file prepared by the author.